Directed electron transport induced surface reconstruction of 2D NiFe-LDH/Stanene heterojunction catalysts for efficient oxygen evolution

Ze Lu [a], Jingkun Wang [a], Pengfei Zhang [a], Wenhao Guo [a], Yongqing Shen [a], Peizhi Liu [a], Jianlong Ji [b], Huayun Du [a], Min Zhao [a,c,*], Haojie Liang [a,**], Junjie Guo [a,**]

[a] *Key Laboratory of Interface Science and Engineering in Advanced Materials of Ministry of Education, College of Materials Science and Engineering, Taiyuan University of Technology, Taiyuan, Shanxi 030024, China*
[b] *College of Electronic Information and Optical Engineering, Taiyuan University of Technology, Taiyuan, Shanxi 030024, China*
[c] *Aluminum-Magnesium Based New Material R&D Co., Ltd., Subsidiary of Xing Xian County Economic and Technological Development Zone, Xing Xian County 033600, China*

ARTICLE INFO

ABSTRACT

As promising non-noble candidates for oxygen evolution reaction (OER), NiFe-based layered double hydroxides (NiFe-LDH) has been proven to transform into its high-oxidation-state Ni/Fe oxyhydroxide, which act as the primary active sites. However, advancing the emergence of high-oxidation-state Ni/Fe oxyhydroxide during OER process currently remains a challenge. Herein, a novel 2D NiFe-LDH/stanene p-n junction catalyst is achieved by inserting stanene between NiFe-LDH and Ni foam. In-situ Raman spectra and density functional theory calculations (DFT) confirm that stanene not only benefits for the construction of built-in electric field, but also serves as an electron absorber to induce a directed electron transport from Ni, Fe to Sn, which thus facilitates the surface reconstruction to form the catalytically active Ni/FeOOH. Consequently, an ultralow OER overpotential (230 mV) at 100 mA cm^{-2} is achieved, corresponding to a considerable decrease of 22.3% and 42.1% compared with the individual NiFe-LDH and stanene, respectively. This work provides a promising avenue for the development of efficient OER catalysts for water electrolysis.

1. Introduction

Electrochemical water splitting plays a vital role in the realm of energy transformationin and storage technologies [1,2]. Nevertheless, the oxidative half reaction of water splitting, referred to the oxygen evolution reaction (OER), processes sluggish kinetics due to its four-electron redox processes, and thus requires higher potentials to obtain more energy for the reaction [3–6]. Currently, IrO$_2$ [7] and RuO$_2$ [8,9] catalysts are considered to be the benchmark electrocatalysts for OER, but the cost and reserves limit their wide applications [10]. Thus, there exists an imperative need to devise non-noble metal electrocatalysts with boosted catalytic performance at low overpotentials to replace noble metal catalysts [11].

In an effort to augment the OER performance of non-noble catalysts, a host of strategies have been devised such as composition tuning [12, 13], heteroatom doping [14,15] and defect engineering [16,17]. Among

these, heterointerface engineering [18–21] is considered as one of the most effective strategies, mainly due to that the reconfiguration of electrons at the heterojunction interface favors electron transfer at the electrode surface [22–24]. For instance, He et al. developed positively charged FeNi-LDH by constructing a p-n structure, resulting in an excellent electrocatalytic performances for OER with an overpotential of 254 mV at 100 mA cm^{-2} [25]. Zeng et al. investigated the construction of p-n junctions between MnCo-CH and NiFe-OH, which greatly enhanced electrocatalytic activity (250 mV@100 mA cm^{-2}). Moreover, the alkaline electrolyzer based on MnCo-CH@NiFe-OH was able to be driven stably at a low voltage of only 1.69 V for 100 mA cm^{-2} [26]. As a promising candidate for OER, NiFe-LDH is a typical n-type semiconductor. During OER, the transition metals, such as Ni^{2+}, undergo a transformation into high-oxidation-state species, specifically NiOOH with an oxidation state of Ni greater than +3. These high-oxidation-state species are widely acknowledged as the active sites responsible for

---

catalyzing for this reaction [27,28]. Consequently, the enhanced OER kinetics necessitate a decreased onset potential for the generation of the high-oxidation-state Ni(Fe) species.

Two-dimensional single-element stanene has recently emerged as a novel category of electrocatalysts owing to its elevated carrier mobility and abundant active sites on the ultrathin planar configuration [29–31]. As a p-type semiconductor, once it contacts with NiFe-LDH to construct a p-n junction, the positively charged NiFe-LDH contributes to the adsorption of OH^-, which is expected to promote the phase transition ($Ni^{2+}(OH)_2 \rightarrow Ni^{3+\delta}OOH$) and thus improve the electrocatalytic activity. Inspired by this idea, 2D p-n heterojunctions catalyst with an optimal electronic structure transition for alkaline OER was engineered by coupling the liquid-exfoliated 2D stanene nanosheets (Sn NSs) with the NiFe-LDH via electrodeposition. X-ray photoelectron spectroscopy (XPS) demonstrated the interaction between Sn and Fe atoms at the heterogeneous interface, which modulated the electron distribution proximate to the interface and notably enhanced the intrinsic catalytic activity of the catalyst. Mott-Schottky (M-S) tests, in-situ Raman and DFT calculations confirmed that the p-n junction directed electron transference from Ni, Fe to Sn, thus promoting the surface reconstruction of NiFe-LDH/Sn NSs and optimizing the d-band center. Consequently, NiFe-LDH/Sn NSs in alkaline electrolyte can stably drive 100 mA cm^{-2} at a low overpotential of 230 mV (relative to RHE). Our work highlights an unequivocal influence of the Sn NSs in fostering the oxidation state transition of Ni, offering new vistas for engineering efficient OER catalysts towards enhanced feasibility of electrochemical water-splitting applications.

2. Experimental

2.1. Synthesis of Sn NSs

Two-dimensional Sn NSs were synthesized by a combination of low-temperature exfoliation and ice-bath liquid-phase exfoliation. In detail, 500 mg of Sn powder was ground in agate mortar for 30 minutes and then transferred to 100 mL of DMF solution. Subsequently, the Sn powder solution was sonicated for 6 h in an ice-bath at 500 W with ultrasound probe 2 s pulses. The solution was centrifuged at 3000 rpm for 5 minutes to remove the oversized masses and the supernatant was centrifuged at 11000 rpm for 10 minutes and the sediment was dispersed in DMF.

2.2. Synthesis of Sn NSs/NF

Typically, a piece of NF (1 × 3 cm^2) pretreated with 1.0 M HCl, acetone, anhydrous ethanol, and ultrapure water was immersed in a DMF suspension of Sn NSs (0.5 mg mL^{-1}) for 12 h. Then the Sn NSs/NF was dried in vacuum at 60 °C for 12 h.

2.3. Synthesis of NiFe-LDH/Sn NSs/NF

The NiFe-LDH/Sn NSs/NF was made by electrodeposition method. The typical potentiostatic deposition of NiFe-LDH was conducted at a potential of −1.2 V for a duration of 300 s at room temperature using a CHI 760E potentiostat-galvanostat. The electrolyte consists of a mixture of 40 mM Ni(NO$_3$)$_2$·6 H$_2$O and Fe(NO$_3$)$_3$·9 H$_2$O, with a molar ratio of 1:1. To prepare the NiFe-LDH/Sn NSs/NF electrodes, the deposition potential was adjusted within the range of −0.8 to −2.0 V, and the deposition time varied from 60 to 480 seconds. For comparison, NiFe-LDH/NF was produced using a similar method, with the only difference being that the original NF was employed as the working electrode.

2.4. Synthesis of RuO$_2$/NF

A mixture of 15 mg of commercial RuO$_2$ powder, 500 μL of ethano, and 15 μL of Naffon solution (5.0 *wt*.%) was dispersed in 485 μL of H$_2$O.

The solution was ultrasonicated and then drop-casted onto a clean NF.

3. Results and discussion

3.1. Catalysts characterization

The synthesis of NiFe-LDH/Sn NSs is illustrated in Fig. 1a. Firstly, two-dimensional Sn NSs were synthesized by a liquid-phase exfoliation method (Fig. S1). Transmission electron microscopy (TEM) showed the lamellar morphology of Sn NSs and the lattice separation of 0.29 nm, corresponding to the (200) crystal plane of stanene (Fig. S2). X-ray diffraction (XRD) spectroscopy also confirmed the successful exfoliation of stanene nanosheets (Fig. S3). Then the Sn NSs were dispersed on the NF (noted as Sn NSs/NF), accompanied by the obvious color change of NF from silver to black (Fig. S4). Scanning electron microscopy (SEM) examination revealed that Sn NSs were uniformly covered on the macroporous NF (Fig. S5). Next, ultra-thin NiFe-LDH nanosheets were electrodeposited onto the Sn NSs/NF using constant voltage technology in aqueous solutions containing Ni^{2+} and Fe^{3+}, noted as NiFe-LDH/Sn NSs/NF. The deposition of NiFe-LDH/Sn NSs/NF was confirmed by XRD (Fig. 1b). Distinctive peaks of Sn NSs were evidently visible on NiFe-LDH/Sn NSs/NF. Due to the lower crystallinity, NiFe-LDH/Sn NSs/ NF and NiFe-LDH/NF exhibited weak NiFe-LDH diffraction peaks [32].

SEM image of the NiFe-LDH/Sn NSs/NF heterostructure showed a uniformly interconnected nanosheets array, which exhibited similar morphology as pure NiFe-LDH (Figs. 1c and S6). TEM images of the NiFe-LDH/Sn NSs further revealed that NiFe-LDH was uniformly coated on the Sn NSs (Fig. S7). High-resolution TEM (HRTEM) image is depicted in Fig. 1d, the NiFe-LDH/Sn NSs interface marked by brownish dashed lines can be clearly observed. The yellow rectangular region and the blue rectangular region possessed lattice stripes with face spacing of 0.29 nm and 0.25 nm can be assigned to Sn NSs (200) and NiFe-LDH (012), respectively. Energy-dispersive X-ray spectroscopy (EDX) mapping showed that the elements Fe, Ni, O, and Sn were homogenously distributed on NiFe-LDH/Sn NSs (Fig. 1e). Furthermore, it can be inferred that Sn NSs were covered by NiFe-LDH.

Surface chemical states of the synthesized catalysts were examined using XPS. The survey spectra indicated the existence of Ni, Fe, O, and Sn on the catalyst surface (Fig. S8), which corroborated with the element mapping analysis. As illustrated in Fig. 2a for the Ni 2p spectra, the peaks of 855.9 eV and 873.5 can assign to Ni 2p$_{3/2}$ and Ni 2p$_{1/2}$ orbitals of Ni^{2+} [33]. The peaks observed at 714.5 eV and 727.7 eV were ascribed to the Fe 2p$_{3/2}$ and Fe 2p$_{1/2}$ orbitals of Fe^{3+}, whereas the peaks at 711.6 eV and 724.8 eV were associated with Fe 2p$_{3/2}$ and Fe 2p$_{1/2}$ of Fe^{2+} respectively. The other four peaks at 717.5 eV, 721.1 eV (2p$_{3/2}$) and 731.7 eV, 734.6 eV (2p$_{1/2}$) are allocated to satellites (Fig. 2b) [34, 35]. The spectral peaks at 487.7 eV and 496.1 eV were correspond to the Sn 3d$_{5/2}$ and Sn 3d$_{3/2}$ orbitals of Sn^{4+}, and two another peaks at 495.2, 486.8 eV were attributed to Sn^{2+} respectively [36] (Fig. 2c). Following the formation of a heterogeneous interface between NiFe-LDH and Sn NSs, the peaks of Ni 2p$_{1/2}$ and Ni 2p$_{3/2}$ concerning NiFe-LDH/Sn NSs exhibited negligible shift compared to NiFe-LDH. However, the Fe 2p$_{3/2}$ peak of the NiFe-LDH/Sn NSs exhibited a positive shift of 0.6 eV compared to that of the NiFe-LDH. In the contrary, Sn 3d spectra of NiFe-LDH/Sn NSs exhibited a negative shift of 0.4 eV compared to Sn NSs. These results suggested the Fe atoms had a strong interaction with Sn atoms at the interface. Part of Fe electron was transferred to Sn due to the electronegativity difference of between Sn (1.96) and Fe (1.8) [37].

Further investigation was focused on the electron transfer occurring at the interface of NiFe-LDH/Sn NSs. The energy band structure of the samples were examined through UV–visible spectroscopy (UV-Vis) (Fig. S9) and M-S plots [38]. Tauc curves suggested the energy band gaps of Sn NSs and NiFe-LDH were 2.43 and 2.10 eV, respectively (Fig. S10). The M-S curve of NiFe-LDH (Fig. 2d) exhibited a positive slope across varying frequencies, indicative of an exemplary feature of n-type semiconductors. Meanwhile, the M-S curve of Sn NSs (Fig. 2e) showed a
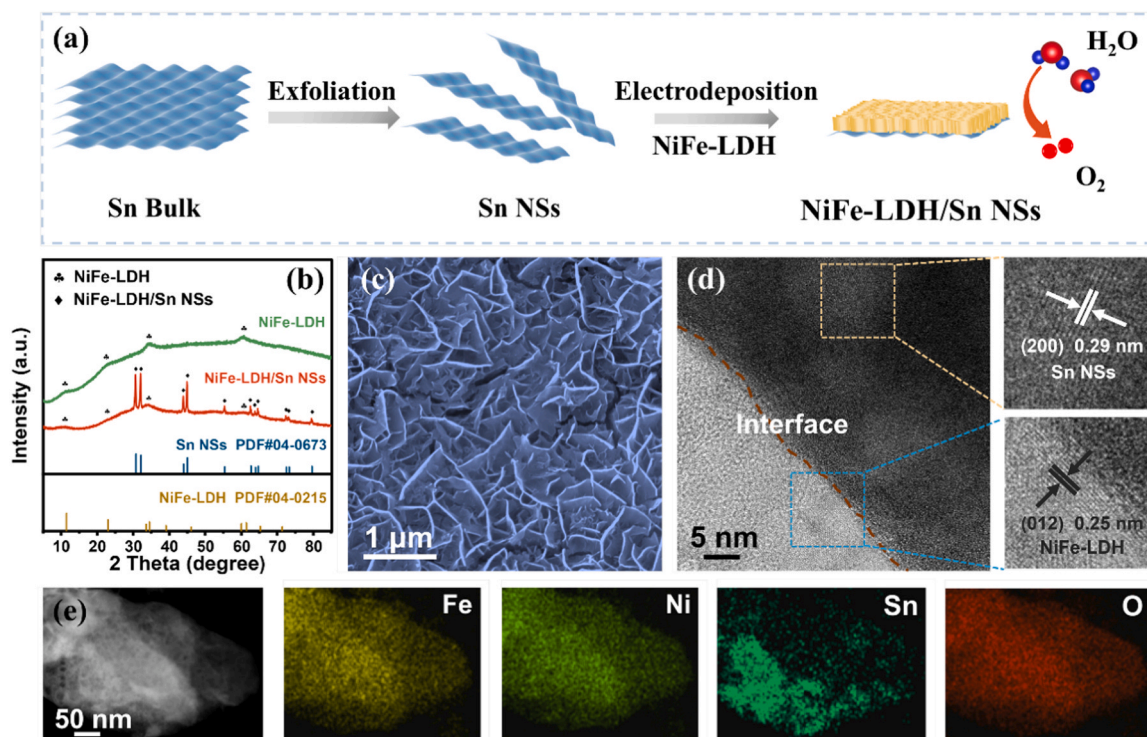
Fig. 1. Fabrication process and structural characterization of 2D NiFe-LDH/Sn NSs heterostructure. (a) Schematic illustration of the synthesis process of NiFe-LDH/Sn NSs, (b) XRD patterns, (c) SEM images of NiFe-LDH/Sn NSs, (d) HRTEM image of NiFe-LDH/Sn NSs, (e) Elemental mapping images of Ni, Fe, Sn and O for NiFe-LDH/Sn NSs.

negative slope, indicating its p-type semiconductor properties. By intersecting the tangent line of the slope with the transverse coordinate, the flat-band potentials (FB) for NiFe-LDH and Sn NSs were found to be 0.27 V and 0.92 V (vs. RHE), respectively. The conduction band potential (V_{CB}) of n-type semiconductors or the valence band potential (V_{VB}) of p-type semiconductors possessed a difference of 0.1 V to the flat band voltage (V_{FB}) [38,39]. By integrating the energy band gap with the positions of E_{CB} and E_{VB}, the energy band structures of NiFe-LDH and Sn NSs were illustrated in Fig. 2f. However, when the n-type NiFe-LDH contacted with p-type Sn NSs, a p-n junction would be formed due to different fermi levels (Fig. S11). Thus, the internal electric field in NiFe-LDH/Sn NSs heterojunction is formed by charge separation between two components in heterojunction. Specifically, the holes near the junction diffused from the p-region to the n-region, while the electrons diffused from the n-region to the p-region. The holes are accumulated on the NiFe-LDH surface while the electrons are concentrated on the Sn NSs facet, and the internal electric field was formed. As results, the formation of holes at the NiFe LDH facilitated OH^- migration in the electrolyte and made it easier to produce $NiFe(OOH)_x$ at the anode, thereby increasing the OER performance [40–42]. Additionally, zeta potential was performed to evaluate the surface charge. As shown in Fig. 2g, the acquired zeta potential of NiFe-LDH/Sn NSs was −14.3 mV, which was 1.94 times higher than that of pure NiFe-LDH (-7.37 mV) [43–45]. Kelvin probe force microscopy (KPFM) was utilized to measure the surface potential of catalysts [43,46]. Fig. 2h and i provides two-dimensional surface potential distribution images of NiFe-LDH and NiFe-LDH/Sn NSs, respectively. The line-scanning surface potential profiles indicated that the contact potential difference (CPD) of NiFe-LDH/Sn NSs was 34.1 mV, much higher than that of NiFe-LDH (15.2 mV). These results further substantiated the successful construction of interfacial electric field, which was expected to enhance the performance of NiFe-LDH/Sn NSs for OER.

3.2. OER performance

The electrochemical performances of prepared catalysts were evaluated through a standard three-electrode setup in 1 M KOH. The influence of voltage and deposition time of NiFe-LDH during preparation were initially investigated. Fig. 3a showed the iR-corrected OER linear scanning voltammetry (LSV) polarization curves of the prepared samples at a low scan rate of 5 mV s^{-1}. The optimal deposition potential was 1.2 V, and the optimal reaction time was 300 s (Fig. S12). The 2D NiFe-LDH/Sn NSs heterostructure exhibited highest OER activity with only a 230 mV overpotential at 100 mA cm^{-2} while the NiFe-LDH, Sn NSs, NF, and RuO$_2$ necessitated overpotentials of 296, 397, 408, and 354 mV at 100 mA cm^{-2}, respectively (Fig. 3b). The LSV result of NiFe-LDH/Sn NSs showed a small oxidation peak compared to pure NiFe-LDH, which resulted from the introduction of Sn NSs accelerating the electron transport in the built-in electric field and the transition of the active phase, thus accelerating the oxidation of LDH. The activity of 2D NiFe-LDH/Sn NSs heterostructure was also superior to the reported OER electrocatalysts in alkaline media of the identical category, which were outlined in Fig. 3h and Table S1.

To reveal the kinetic behavior of 2D NiFe-LDH/Sn NSs heterostructure, the Tafel slopes were calculated (Fig. 3c). 2D NiFe-LDH/Sn NSs heterostructure displayed the lowest Tafel slope (35 mV dec^{-1}) compared to RuO$_2$ (51 mV dec^{-1}), NiFe-LDH (57 mV dec^{-1}), and Sn NSs (64 mV dec^{-1}), which suggested a faster reaction kinetics. Next, the electrochemical active surface area (ECSA) of each samples were calculated from electrochemical bilayer capacitance (C_{dl}) by examining the CV curves in the non-Faraday current region at varying scan rates (20–100 mV s^{-1}) (Fig. S13). As depicted in Fig. 3d, the C_{dl} of the 2D NiFe-LDH/Sn NSs heterostructure is 7.65 mF cm^{-2}, which was obviously larger than that of NiFe-LDH (6.87 mF cm^{-2}). The Sn NSs catalyst (with a capacitance value of 7.82 mF cm^{-2}) exhibited a larger C_{dl} value, suggesting it possessed abundant active sites for electrochemical reactions. However, the Sn NSs showed low activity for the OER reaction,
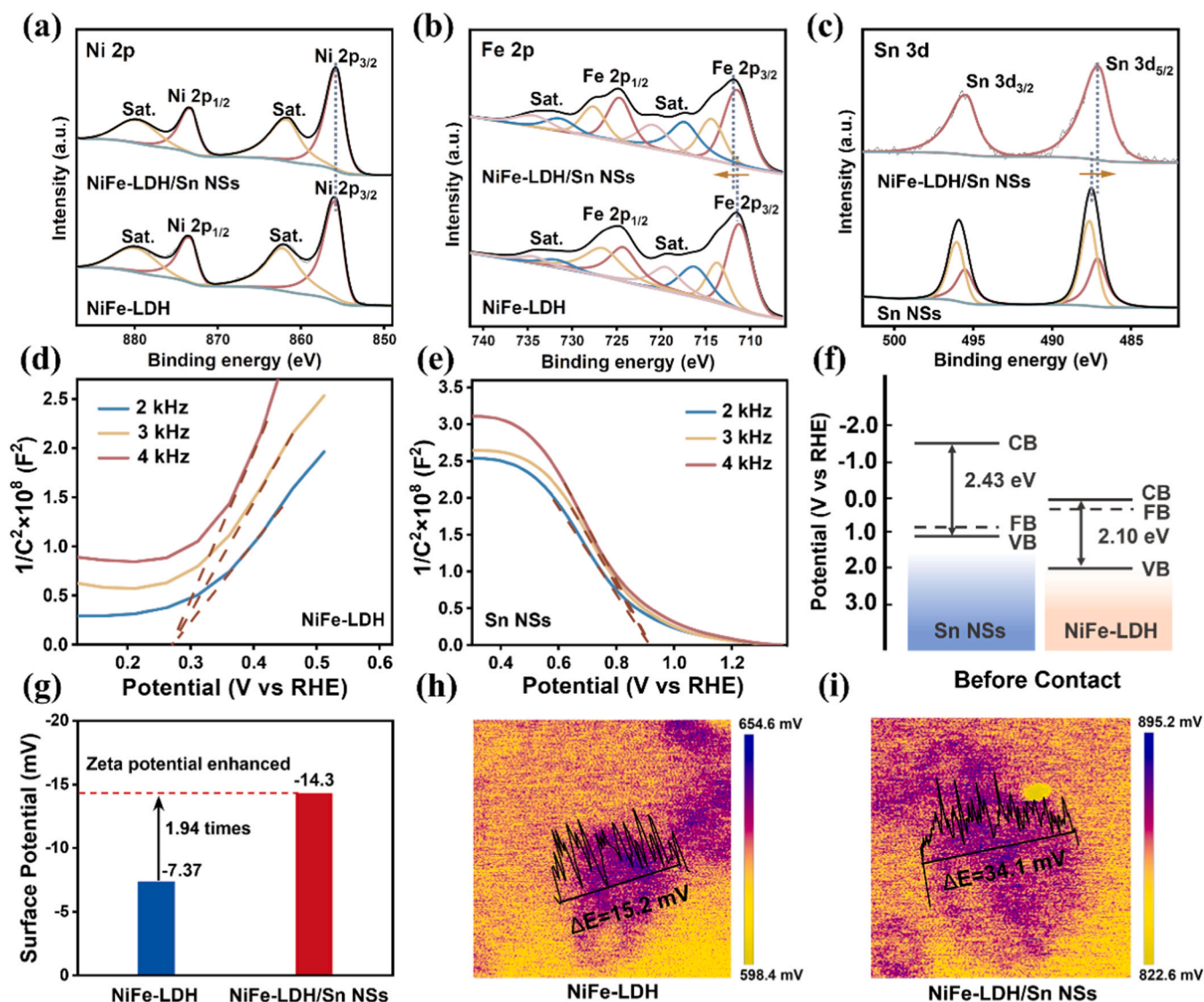
Fig. 2. Surface chemical structure and energy level structure of 2D NiFe-LDH/Sn NSs. The high-resolution XPS spectra of (a) Ni 2p, (b) Fe 2p, (c) Sn 3d for NiFe-LDH and NiFe-LDH/Sn NSs. M-S plots of the (d) NiFe-LDH and (e) Sn NSs at various frequencies. (f) Energy band diagram of NiFe-LDH and Sn NSs. (g) The zeta potentials of NiFe-LDH and NiFe-LDH/Sn NSs. (h, i) KPFM potential images and the corresponding surface potential.

which may result from that not all of electroactive sites counted by ECSA performed high OER activity [47]. Nyquist plots were recorded under the equivalent circuit to further investigate charge transfer of each sample (Fig. 3e, Table S2). According to the Nyquist plots, the 2D NiFe-LDH/Sn NSs heterostructure exhibited the smallest charge transfer resistance (R_{ct}), indicating an enhanced electron transfer kinetics. All these results evidenced that the 2D NiFe-LDH/Sn NSs heterostructure exhibited the advantages of increased active sites and enhanced electron transfer attributed to the internal electric field at the interface, which then resulted in improved reaction kinetic and significantly reduced overpotentials in comparison with the individual 2D NiFe-LDH and 2D Sn NSs.

To test the applicability of this strategy, we prepared NiFe-LDH/Sn NSs and pure NiFe-LDH catalysts by the same method using carbon cloth (CC) and iron foam (IF) as substrate, respectively. SEM image of the NiFe-LDH/Sn NSs/CC heterostructure showed a uniformly interconnected nanosheets array, which exhibited similar morphology as NiFe-LDH/Sn NSs/NF (Fig. S14a). For the IF substrate, it was also observed that the surface of the nanosheets was rougher than that on the NF substrate (Fig. S14c). As with the previous test method, the electrochemical performances of prepared catalysts were evaluated through

a standard three-electrode setup in 1 M KOH. Fig. S14b and d shows the iR-corrected LSV polarisation curves of the two samples. It can be observed that the 2D heterostructured NiFe-LDH/Sn NSs exhibit significantly lower overpotentials compared to pure NiFe-LDH on both substrates. These results further suggested the key role of Sn NSs.

The cycle stability of the 2D NiFe-LDH/Sn NSs heterostructure catalyst was further verified through continuous cyclic voltammetry (CV) cycles. The polarization curve (Fig. 3f) obtained after 2000 cycles was nearly overlapped with the initial polarization curve, indicating that the catalyst possessed good cycle performance [48]. Fig. 3g showed that at an elevated current density of 100 mA cm^{-2}, the catalyst exhibited no significant decay even after 60 hours, indicating excellent OER endurance in alkaline solutions. Following the OER stability test, the alteration of the surface topography and architecture of 2D NiFe-LDH/Sn NSs heterostructure catalyst were also examined. As displayed in Fig. S15, the morphology exhibited scarcely any change, therefore providing further evidence of the exceptional structural stability of 2D NiFe-LDH/Sn NSs catalyst.
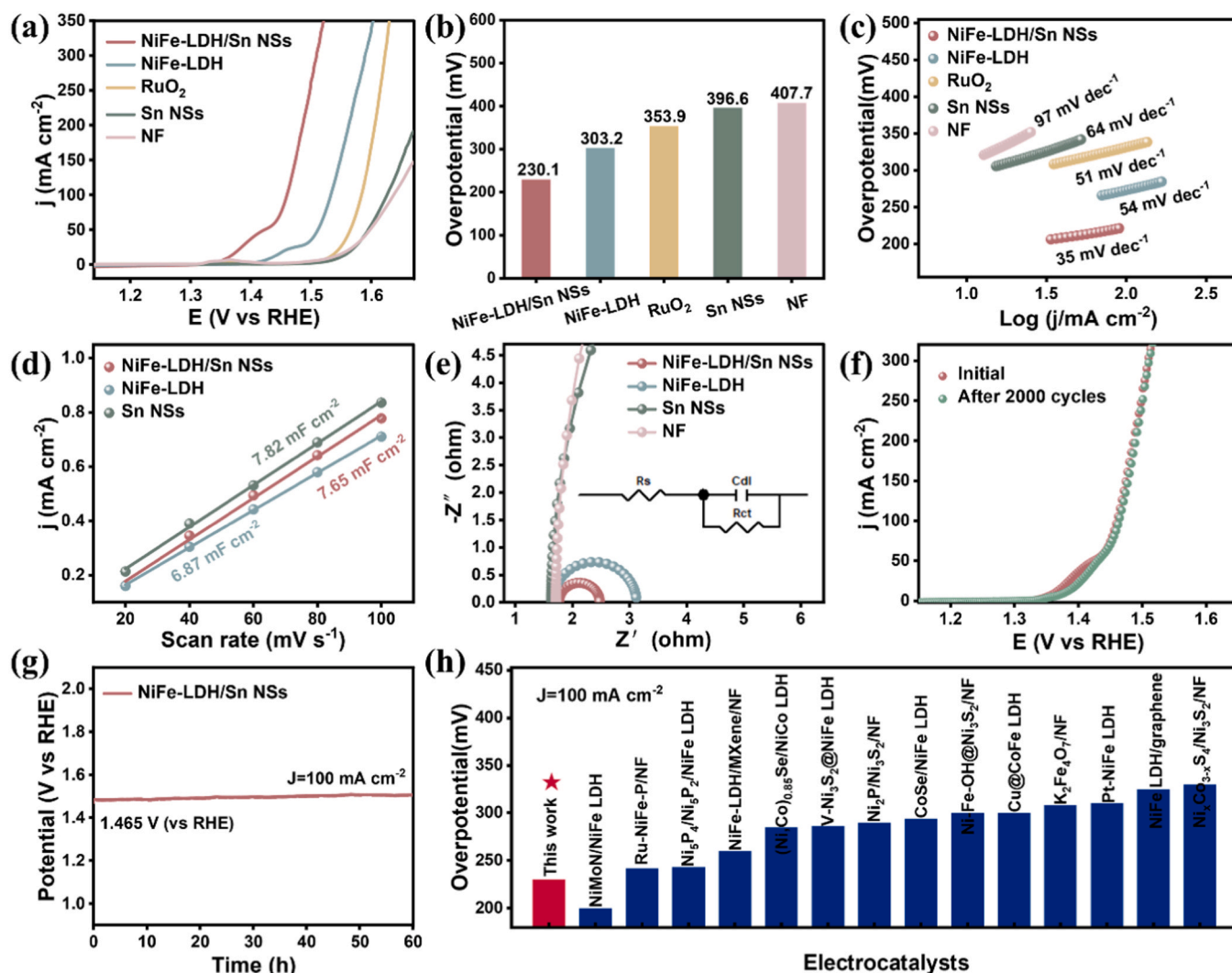
Fig. 3. Electrochemical measurements. (a) Polarization curves, (b) Related overpotential at 100 mA cm^{-2}, and (c) Corresponding tafel curves for commercial RuO$_2$, Sn NSs, NiFe-LDH, NF and NiFe-LDH/Sn NSs heterojunction in KOH (1 M) electrolytes, respectively; (d) Plots showing the extracted C$_{dl}$ value to estimate the ECSA, (e) EIS Nyquist plots of Sn NSs, NiFe-LDH, NiFe-LDH/Sn NSs and NF; (f) OER polarization curves of NiFe-LDH/Sn NSs before and after 2000 CV cycles test at 1 M KOH, (g) Chronopotentiometry curves of NiFe-LDH/Sn NSs for 60 h for the OER, (h) Comparison with reported OER catalysts.

3.3. Overall water splitting performance and mechanism analysis

To explore the application of overall water electrolysis, we assembled a two-electrode electrolyzer utilizing prepared 2D NiFe-LDH/Sn NSs heterostructure as the anode and Pt foil as the reference cathode (Fig. S16). Notably, as depicted in Fig. 4a, the NiFe-LDH/Sn NSs ∥ Pt electrolyzer exhibited remarkable overall water splitting activity in 1.0 M KOH. A battery potential of 1.52 V was needed to attain a current density of 10 mA cm^{-2}, significantly beneath the benchmark for commercial RuO$_2$ ∥ Pt (1.63 V). The gaseous products of water electrolysis on a NiFe-LDH/Sn NSs ∥ Pt electrolyzer at 100 mA cm^{-2} were measured using a gas chromatograph. As shown in Fig. 4b, the ratio of gas volume generated at the cathode and anode corresponded closely to the theoretical value of 2:1, demonstrating that the 2D NiFe-LDH/Sn NSs heterostructure catalyst exhibited an almost 100% Faraday efficiency in overall water splitting. Moreover, the NiFe-LDH/Sn NSs ∥ Pt electrolyzer was subjected to a 24 h stability test in a 1 M KOH electrolyte at an elevated current density of 100 mA cm^{-2} and exhibited no significant decay (Fig. 4c). These achievements notably prove the 2D NiFe-LDH/Sn NSs heterostructure catalyst is an ideal candidate for water-splitting process with low expenditure, superior performance and robust stability.

Utilizing electrochemical methanol oxidation as an alternative to OER not only mitigates the energy wastage during water disintegration, but also generates formate as a valuable by-product [49]. As illustrated in Fig. S17, when utilizing a blend of 0.5 M methanol and 1 M KOH as the electrolyte, the resulting potential for 2D NiFe-LDH/Sn NSs heterostructure catalyst at a current density of 100 mA cm^{-2} was merely 1.419 V (vs. RHE), which was appreciably lower than the potential of 1.46 V (vs. RHE) in 1 M KOH. This indicated that the addition of methanol to the 1 M KOH solution would lead to a lower energy consumption. When the current density reached 10 mA cm^{-2} and 100 mA cm^{-2}, 2D NiFe-LDH/Sn NSs heterostructure catalyst demonstrated superior performance compared to Sn NSs and NiFe LDH (Fig. S18), and it can be observed that Sn NSs play a crucial role. As presented in Fig. S19, 2D NiFe-LDH/Sn NSs heterostructure catalyst demonstrated superior performance compared to both the Sn NSs and NiFe-LDH catalysts in the methanol oxidation reaction. Specifically, the former exhibited superior kinetics, a larger effective surface, and a lower charge transfer resistance. Fig. S20 presented the cyclic voltammetry curve for the non-Faraday current region at different scan rates (20–100 mV s^{-1}) obtained from the methanol oxidation reaction. The catalyst was subsequently subjected to stability testing at 100 mA cm^{-2}, with no noticeable attenuation even after 48 hours. These results
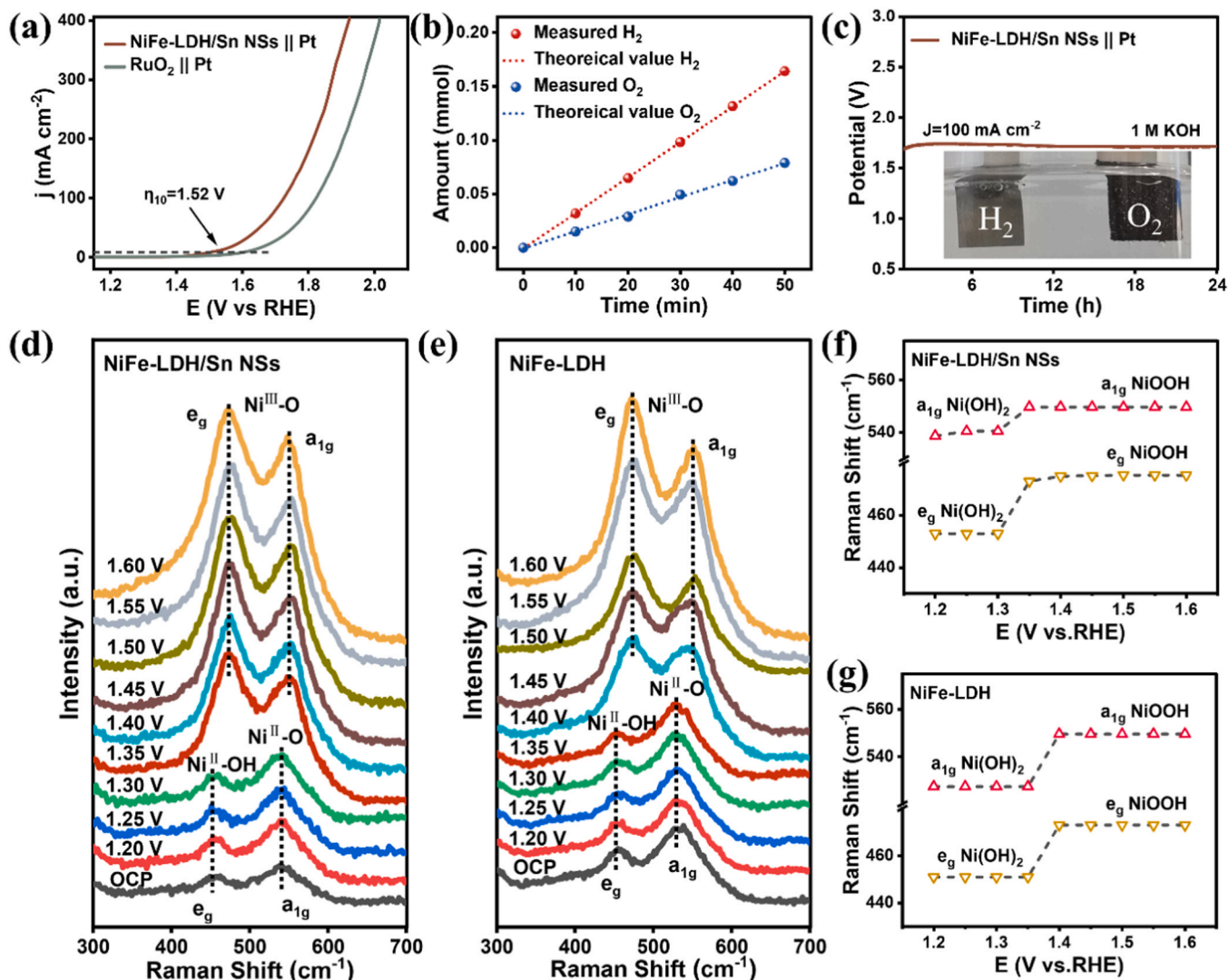
Fig. 4. Overall water splitting performance and mechanism analysis. (a) Polarization curves in 1 M KOH of electrolytic cells using different anodes of NiFe-LDH/Sn NSs, benchmark RuO₂ with same Pt foil as cathodes. (b) Generated H₂ and O₂ amounts for the assembled electrolyzer at 10 mA cm⁻². (c) Time-dependent voltage curves at constant currents of 100 mA cm⁻² for 24 h. Potential-dependent in-situ Raman spectra of OER process (d) 2D NiFe-LDH/Sn NSs heterostructure and (e) NiFe-LDH in 1 M KOH. (f, g) Raman peaks' shifts of 2D NiFe-LDH/Sn NSs heterostructure and NiFe-LDH at varying potentials.

indicated that the catalyst exhibited exceptional durability in a solution comprising 0.5 M methanol and 1 M KOH (Fig. S21).

The electrochemical in-situ Raman spectroscopy was investigated to elaborate the active structures of 2D NiFe-LDH/Sn NSs heterostructure catalyst for the OER (Fig. 4d, e). At open circuit potential, 2D NiFe-LDH/Sn NSs and NiFe-LDH displayed distinctive peaks at 451 and 538 cm⁻¹, which were attributed to the e_g bending (Ni^{II}-OH) and a_{1g} stretching (Ni^{II}-O) vibrations of Ni(OH)₂, respectively [50,51]. For 2D NiFe-LDH/Sn NSs, two distinctive spectral peaks emerged at 475 and 551 cm⁻¹ beyond 1.35 V (Fig. 4f), reflecting the e_g bending (δ Ni^{III}-O) and a_{1g} stretching (ν Ni^{III}-O) vibrational modes, respectively [28]. Raman spectra of NiFe-LDH/Sn NSs before and after cycle stability test are shown in Fig. S22, and the Fe-O vibration of FeOOH was observed at 679.8 cm⁻¹, indicating the existence of FeOOH [27,52]. After cycle stability test, the Fe-O peak diminished significantly, which can be attributed to that the Fe is incorporated into the NiOOH lattice to form active Ni/FeOOH species [28,53]. Significant analogous Raman peaks emerged until the potential reached 1.4 V for NiFe-LDH (Fig. 4g). Furthermore, the elevated I_{551}/I_{475} ratio of 2D NiFe-LDH/Sn NSs compared to NiFe-LDH at 1.6 V is attributed to β-NiOOH [54]. Consequently, the generation of reactive species was facilitated for the

as-activated 2D NiFe-LDH/Sn NSs heterostructure catalyst, encouraging the attainment of an optimum electronic structure for OER.

XPS spectra and in-situ Raman spectra of NiFe-LDH/Sn NSs after 2000 th CV scan were recorded to evaluate the elemental electronic states (Fig. S23). The high-resolution spectra of Ni $2p_{3/2}$ exhibits three prominent peaks, with 855.7 eV (Ni^{2+}) and 856.8 eV (Ni^{3+}) assigned to Ni–O bonds and a satellite peak at 861.9 eV [55,56]. A positive shift in the binding energy is observed, indicating the emergence of higher valence states for Ni. Meanwhile, the major peak of the Fe 2p shifts to higher potential energy than the pristine electrocatalyst, manifesting the oxidation state of Fe. Moreover, Sn 3d spectra of exhibited a negative shift compared to the initial NiFe-LDH/Sn NSs, indicating an electrons enrichment of Sn NSs. The XPS results suggest that the surface metal species have been re-arranged and oxidized during OER [26,28]. After 2000 th CV cycles, negligible changes could be observed for the bands at 475 and 551 cm⁻¹ when increasing the applied potentials from 1.20 to 1.60 V, illustrating that the crystal phase of NiOOH was stable and the phase transformation was irreversible. As given in Fig. 3f, the polarization curves after 2000 CV are almost overlapped, further demonstrating the excellent stability of NiFe-LDH/Sn NSs after reconstruction. In addition, combined the XPS and Raman results demonstrate that

electrons were directional transfer from Ni, Fe to Sn. The internal Sn NSs serves as a swift transmission channel for electrons, while the external Ni/FeOOH serves as the actual active center during OER.

3.4. Theoretical analysis

To further explore the electronic structure of the interface between NiFe-LDH/Sn NSs and unravel their role in promoting OER catalytic activities, we conducted DFT calculations. The geometrical models of the heterostructures of Sn NSs, NiFe-LDH and NiFe-LDH/Sn NSs were constructed by combining the HRTEM, XPS, XRD and Raman results. And the electron transfer behavior was delineated quantitatively via computation of the disparity in charge density, wherein the yellow and cyan areas signify the electron accumulation and depletion zones, respectively (Fig. 5a). Evidently, the introduced Sn NSs resulted in local charge redistribution at the interface and triggered electron migration from NiFe-LDH to Sn NSs, aligning with the findings of XPS. The projected density of states (PDOS) of Sn NSs, NiFe-LDH, and NiFe-LDH/Sn NSs were calculated to understand the relationship between the structure and d-band center (Fig. 5b). The ε_d value for NiFe-LDH/Sn NSs showed an increase from -1.89 eV to -1.73 eV, as compared to pure NiFe-LDH, which intensified the interactions between the nickel sites and the oxygen intermediates.

Subsequently, the adsorption free energies of oxygen intermediates were calculated (Figs. S24–S26). The curve of free energy change (Fig. 5c) represented the reaction step at U = 1.23 V. For Sn NSs, the generation of activated *OOH intermediates emerged as the rate-limiting step (RDS), with an energy barrier of 1.87 eV. NiFe-LDH revealed superior catalytic kinetics with certain oxygen binding potency, and the conversion of *OOH to O_2 became the RDS ($\Delta G =$ 1.56 eV). Furthermore, for NiFe-LDH/Sn NSs, the RDS shifted to the conversion of *OH to *O ($\Delta G = 0.65$ eV), which indicated that NiFe-LDH/Sn NSs were thermodynamically more favorable for OER (Fig. 5d). The DFT results were consistent with the activity measurements, indicating that the constructed 2D NiFe-LDH/Sn NSs heterostructure catalyst can effectively optimize the electronic structure of the catalyst, reduce the reaction energy barrier, and accelerate the reaction kinetics.

4. Conclusion

In this work, we prepared a high-performance 2D NiFe-LDH/Sn NSs p-n heterostructure catalyst, which exhibited excellent electrocatalytic OER activity (230 mV@100 mA cm^{-2}) and stability, surpassing the majority of the previously reported electrocatalysts. XPS, Mott-Schottky analysis, KPFM and in-situ Raman suggested that built-in electric field was capable of accelerating electron-directed transport and inducing surface reconstruction. Results from DFT simulations have indicated that electron-directed transport modulated the d-band center, thereby optimizing the adsorption and desorption of the intermediate states. Furthermore, the electron-directed transport significantly reduced the Gibbs free energy barrier of the determining step in the OER, leading to enhanced OER performance. This study presents ideas for the rational design of highly efficient and low-energy-consuming stanene-based electrocatalysts.

CRediT authorship contribution statement

Ze Lu: Conceptualization, Validation, Data curation, Writing – original draft. **Jingkun Wang:** Data curation, Software, Visualization. **Pengfei Zhang:** Formal analysis, Validation. **Wenhao Guo:** Validation, Investigation. **Yongqing Shen:** Validation, Investigation. **Peizhi Liu:**
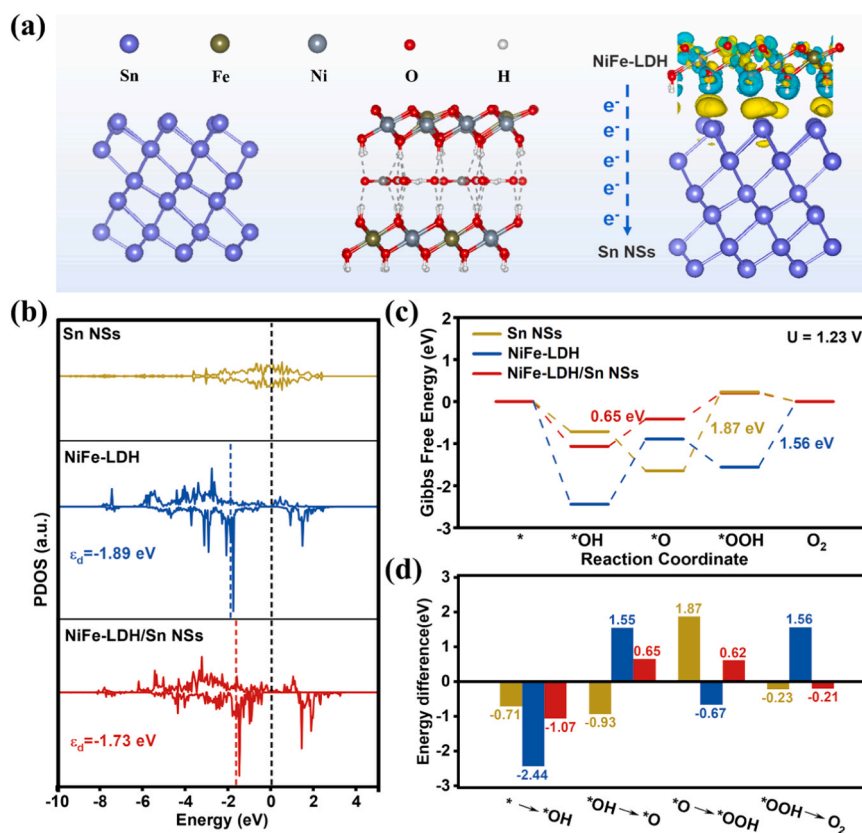
Fig. 5. DFT calculation. (a) The theoretical models of the optimized configurations of Sn NSs, NiFe-LDH, and Charge density difference plot at the NiFe-LDH/Sn NSs interface. (b) The calculated projected density on d orbital for Sn NSs, NiFe-LDH, and NiFe-LDH/Sn NSs. (c) The energetic pathway of OER in the alkaline environment under the applied potential of 1.23 V. (d) Comparision of free energy of different elementary steps in OER on Sn NSs, NiFe-LDH, and NiFe-LDH/Sn NSs.

Validation, Resources. **Jianlong Ji:** Resources. **Huayun Du:** Resources. **Min Zhao:** Project administration, Writing – review & editing, Funding acquisition, Supervision. **Haojie Liang:** Writing – review & editing, Funding acquisition, Supervision. **Junjie Guo:** Writing – review & editing, Funding acquisition, Supervision.

Declaration of Competing Interest

The authors declare that they have no known competing financial interests or personal relationships that could have appeared to influence the work reported in this paper.

Data availability

Data will be made available on request.

Acknowledgment

Appendix A. Supporting information

Supplementary data associated with this article can be found in the online version at doi:10.1016/j.apcatb.2024.124073.

References

[1] P. Prabhu, V.-H. Do, C.K. Peng, H. Hu, S.-Y. Chen, J.-H. Choi, Y.-G. Lin, J.-M. Lee, Oxygen-bridged stabilization of single atomic W on Rh metallenes for robust and efficient pH-universal hydrogen evolution, ACS Nano 17 (2023) 10733–10747, https://doi.org/10.1021/acsnano.3c02066.

[2] J. Mei, J. Shang, T. He, D. Qi, L. Kou, T. Liao, A. Du, Z. Sun, 2D/2D black phosphorus/nickel hydroxide heterostructures for promoting oxygen evolution via electronic structure modulation and surface reconstruction, Adv. Energy Mater. 12 (2022) 2201141, https://doi.org/10.1002/aenm.202201141.

[3] V. Do, P. Prabhu, V. Jose, T. Yoshida, Y. Zhou, H. Miwa, T. Kaneko, T. Uruga, Y. Iwasawa, J. Lee, Pd–PdO nanodomains on amorphous Ru metallene oxide for high-performance multifunctional electrocatalysis, Adv. Mater. 35 (2023) 2208860, https://doi.org/10.1002/adma.202208860.

[4] Y. Song, M. Song, P. Liu, W. Liu, L. Yuan, X. Hao, L. Pei, B. Xu, J. Guo, Z. Sun, Fe-doping induced localized amorphization in ultrathin α-Ni(OH)₂ nanomesh for superior oxygen evolution reaction catalysis, J. Mater. Chem. A 9 (2021) 14372–14380, https://doi.org/10.1039/D1TA02341A.

[5] M. Li, X. Wang, K. Liu, H. Sun, D. Sun, K. Huang, Y. Tang, W. Xing, H. Li, G. Fu, Reinforcing Co-O covalency via Ce(4f)-O(2p)-Co(3d) gradient orbital coupling for high-efficiency oxygen evolution, Adv. Mater. 35 (2023) 2302462, https://doi.org/10.1002/adma.202302462.

[6] S.L.D. Nicole, Y. Li, W. Xie, G. Wang, J. Lee, Heterointerface and tensile strain effects synergistically enhances overall water-splitting in Ru/RuO₂ aerogels, Small 19 (2023) 2206844, https://doi.org/10.1002/smll.202206844.

[7] Y. Ping, R.J. Nielsen, W.A. Goddard, The reaction mechanism with free energy barriers at constant potentials for the oxygen evolution reaction at the IrO₂ (110) surface, J. Am. Chem. Soc. 139 (2017) 149–155, https://doi.org/10.1021/jacs.6b07557.

[8] V. Jose, V.D. Do, P. Prabhu, C. Peng, S. Chen, Y. Zhou, Y. Lin, J. Lee, Activating amorphous Ru metallenes through Co integration for enhanced water electrolysis, Adv. Energy Mater. 13 (2023) 2301119, https://doi.org/10.1002/aenm.202301119.

[9] K.A. Stoerzinger, O. Diaz-Morales, M. Kolb, R.R. Rao, R. Frydendal, L. Qiao, X. R. Wang, N.B. Halck, J. Rossmeisl, H.A. Hansen, T. Vegge, I.E.L. Stephens, M.T. M. Koper, Y. Shao-Horn, Orientation-dependent oxygen evolution on RuO₂ without lattice exchange, ACS Energy Lett. 2 (2017) 876–881, https://doi.org/10.1021/acsenergylett.7b00135.

[10] Y. Huang, M. Li, F. Pan, Z. Zhu, H. Sun, Y. Tang, G. Fu, Plasma-induced Mo-doped Co₃O₄ with enriched oxygen vacancies for electrocatalytic oxygen evolution in water splitting, Carbon Energy 5 (2023) e279, https://doi.org/10.1002/cey2.279.

[11] H. Wang, J. Li, K. Li, Y. Lin, J. Chen, L. Gao, V. Nicolosi, X. Xiao, J.-M. Lee, Transition metal nitrides for electrochemical energy applications, Chem. Soc. Rev. 50 (2021) 1354–1390, https://doi.org/10.1039/D0CS00415D.

[12] B. Zhang, L. Wang, Z. Cao, S.M. Kozlov, F.P. García De Arquer, C.T. Dinh, J. Li, Z. Wang, X. Zheng, L. Zhang, Y. Wen, O. Voznyy, R. Comin, P. De Luna, T. Regier, W. Bi, E.E. Alp, C.-W. Pao, L. Zheng, Y. Hu, Y. Ji, Y. Li, Y. Zhang, L. Cavallo, H. Peng, E.H. Sargent, High-valence metals improve oxygen evolution reaction performance by modulating 3D metal oxidation cycle energetics, Nat. Catal. 3 (2020) 985–992, https://doi.org/10.1038/s41929-020-00525-6.

[13] B. Zhang, X. Zheng, O. Voznyy, R. Comin, M. Bajdich, M. García-Melchor, L. Han, J. Xu, M. Liu, L. Zheng, F.P. García De Arquer, C.T. Dinh, F. Fan, M. Yuan, E. Yassitepe, N. Chen, T. Regier, P. Liu, Y. Li, P. De Luna, A. Janmohamed, H.L. Xin, H. Yang, A. Vojvodic, E.H. Sargent, Homogeneously dispersed multimetal oxygen-evolving catalysts, Science 352 (2016) 333–337, https://doi.org/10.1126/science.aaf1525.

[14] H. Wang, J. Chen, Y. Lin, X. Wang, J. Li, Y. Li, L. Gao, L. Zhang, D. Chao, X. Xiao, J. Lee, Electronic modulation of non-van der waals 2D electrocatalysts for efficient energy conversion, Adv. Mater. 33 (2021) 2008422, https://doi.org/10.1002/adma.202008422.

[15] Y. Dou, C.-T. He, L. Zhang, H. Yin, M. Al-Mamun, J. Ma, H. Zhao, Approaching the activity limit of CoSe₂ for oxygen evolution via Fe doping and Co vacancy, Nat. Commun. 11 (2020) 1664, https://doi.org/10.1038/s41467-020-15498-0.

[16] T. Wu, S. Sun, J. Song, S. Xi, Y. Du, B. Chen, W.A. Sasangka, H. Liao, C.L. Gan, G. G. Scherer, L. Zeng, H. Wang, H. Li, A. Grimaud, Z.J. Xu, Iron-facilitated dynamic active-site generation on spinel CoAl₂O₄ with self-termination of surface reconstruction for water oxidation, Nat. Catal. 2 (2019) 763–772, https://doi.org/10.1038/s41929-019-0325-4.

[17] J. Sun, H. Xue, N. Guo, T. Song, Y. Hao, J. Sun, J. Zhang, Q. Wang, Synergetic metal defect and surface chemical reconstruction into NiCo₂S₄/ZnS heterojunction to achieve outstanding oxygen evolution performance, Angew. Chem. Int. Ed. 60 (2021) 19435–19441, https://doi.org/10.1002/anie.202107731.

[18] Z. Zhang, P. Liu, Y. Song, Y. Hou, B. Xu, T. Liao, H. Zhang, J. Guo, Z. Sun, Heterostructure engineering of 2D superlattice materials for electrocatalysis, Adv. Sci. 9 (2022) 2204297, https://doi.org/10.1002/advs.202204297.

[19] P. Prabhu, V. Jose, J.-M. Lee, Design strategies for development of TMD-based heterostructures in electrochemical energy systems, Matter 2 (2020) 526–553, https://doi.org/10.1016/j.matt.2020.01.001.

[20] Q. Xu, J. Zhang, H. Zhang, L. Zhang, L. Chen, Y. Hu, H. Jiang, C. Li, Atomic heterointerface engineering overcomes the activity limitation of electrocatalysts and promises highly-efficient alkaline water splitting, Energy Environ. Sci. 14 (2021) 5228–5259, https://doi.org/10.1039/D1EE02105B.

[21] R. Subbaraman, D. Tripkovic, D. Strmcnik, K.-C. Chang, M. Uchimura, A. P. Paulikas, V. Stamenkovic, N.M. Markovic, Enhancing hydrogen evolution activity in water splitting by tailoring Li⁺-Ni(OH)₂-pt interfaces, Science 334 (2011) 1256–1260, https://doi.org/10.1126/science.1211934.

[22] Y. Song, B. Xu, T. Liao, J. Guo, Y. Wu, Z. Sun, Electronic structure tuning of 2D metal (hydr)oxides nanosheets for electrocatalysis, Small 17 (2021) 2002240, https://doi.org/10.1002/smll.202002240.

[23] J. Hou, Y. Sun, Y. Wu, S. Cao, L. Sun, Promoting active sites in core-shell nanowire array as Mott-Schottky electrocatalysts for efficient and stable overall water splitting, Adv. Funct. Mater. 28 (2018) 1704447, https://doi.org/10.1002/adfm.201704447.

[24] K.-X. Zhang, H. Su, H.-H. Wang, J.-J. Zhang, S.-Y. Zhao, W. Lei, X. Wei, X.-H. Li, J.-S. Chen, Atomic-scale Mott-Schottky heterojunctions of boron nitride monolayer and graphene as metal-free photocatalysts for artificial photosynthesis, Adv. Sci. 5 (2018) 1800062, https://doi.org/10.1002/advs.201800062.

[25] K. He, T. TadesseTsega, X. Liu, J. Zai, X. Li, X. Liu, W. Li, N. Ali, X. Qian, Utilizing the space-charge region of the FeNi-LDH/CoP p-n junction to promote performance in oxygen evolution electrocatalysis, Angew. Chem. Int. Ed. 58 (2019) 11903–11909, https://doi.org/10.1002/anie.201905281.

[26] Y. Zeng, Z. Cao, J. Liao, H. Liang, B. Wei, X. Xu, H. Xu, J. Zheng, W. Zhu, L. Cavallo, Z. Wang, Construction of hydroxide pn junction for water splitting electrocatalysis, Appl. Catal. B 292 (2021) 120160, https://doi.org/10.1016/j.apcatb.2021.120160.

[27] Y. Bai, Y. Wu, X. Zhou, Y. Ye, K. Nie, J. Wang, M. Xie, Z. Zhang, Z. Liu, T. Cheng, C. Gao, Promoting nickel oxidation state transitions in single-layer NiFeB hydroxide nanosheets for efficient oxygen evolution, Nat. Commun. 13 (2022) 6094, https://doi.org/10.1038/s41467-022-33846-0.

[28] P. Zhai, C. Wang, Y. Zhao, Y. Zhang, J. Gao, L. Sun, J. Hou, Regulating electronic states of nitride/hydroxide to accelerate kinetics for oxygen evolution at large current density, Nat. Commun. 14 (2023) 1873, https://doi.org/10.1038/s41467-023-37091-x.

[29] S.K. Sahoo, K. Wei, A perspective on recent advances in 2D stanene nanosheets, Adv. Mater. Interfaces 6 (2019) 1900752, https://doi.org/10.1002/admi.201900752.

[30] Y. Xu, B. Yan, H.-J. Zhang, J. Wang, G. Xu, P. Tang, W. Duan, S.-C. Zhang, Large-gap quantum spin hall insulators in tin films, Phys. Rev. Lett. 111 (2013) 136804, https://doi.org/10.1103/PhysRevLett.111.136804.

[31] M. Liao, Y. Zang, Z. Guan, H. Li, Y. Gong, K. Zhu, X.-P. Hu, D. Zhang, Y. Xu, Y.-Y. Wang, K. He, X.-C. Ma, S.-C. Zhang, Q.-K. Xue, Superconductivity in few-layer stanene, Nat. Phys. 14 (2018) 344–348, https://doi.org/10.1038/s41567-017-0031-6.

[32] H. Liang, A.N. Gandi, C. Xia, M.N. Hedhili, D.H. Anjum, U. Schwingenschlögl, H. N. Alshareef, Amorphous NiFe-OH/NiFeP electrocatalyst fabricated at low temperature for water oxidation applications, ACS Energy Lett. 2 (2017) 1035–1042, https://doi.org/10.1021/acsenergylett.7b00206.

[33] Q. Dong, C. Shuai, Z. Mo, N. Liu, G. Liu, J. Wang, H. Pei, Q. Jia, W. Liu, X. Guo, CeO$_2$ nanoparticles@NiFe-LDH nanosheet heterostructure as electrocatalysts for oxygen evolution reaction, J. Solid State Chem. 296 (2021) 121967, https://doi.org/10.1016/j.jssc.2021.121967.

[34] T. Li, Y. Hu, K. Liu, J. Yin, Y. Li, G. Fu, Y. Zhang, Y. Tang, Hollow yolk-shell nanoboxes assembled by Fe-doped Mn$_3$O$_4$ nanosheets for high-efficiency electrocatalytic oxygen reduction in Zn-Air battery, Chem. Eng. J. 427 (2022) 131992, https://doi.org/10.1016/j.cej.2021.131992.

[35] Z. Li, X. Wu, X. Jiang, B. Shen, Z. Teng, D. Sun, G. Fu, Y. Tang, Surface carbon layer controllable Ni$_3$Fe particles confined in hierarchical N-doped carbon framework boosting oxygen evolution reaction, Adv. Powder Mater. 1 (2022) 100020, https://doi.org/10.1016/j.apmate.2021.11.007.

[36] B. Zhang, S. Chen, B. Wulan, J. Zhang, Surface modification of SnO$_2$ nanosheets via ultrathin N-doped carbon layers for improving CO$_2$ electrocatalytic reduction, Chem. Eng. J. 421 (2021) 130003, https://doi.org/10.1016/j.cej.2021.130003.

[37] T. Zhang, J. Du, P. Xi, C. Xu, Hybrids of cobalt/iron phosphides derived from bimetal-organic frameworks as highly efficient electrocatalysts for oxygen evolution reaction, ACS Appl. Mater. Interfaces 9 (2017) 362–370, https://doi.org/10.1021/acsami.6b12189.

[38] S. Wang, B.Y. Guan, X. Wang, X.W.D. Lou, Formation of hierarchical Co$_9$S$_8$@ ZnIn$_2$S$_4$ heterostructured cages as an efficient photocatalyst for hydrogen evolution, J. Am. Chem. Soc. 140 (2018) 15145–15148, https://doi.org/10.1021/jacs.8b07721.

[39] Y.-X. Pan, Y. You, S. Xin, Y. Li, G. Fu, Z. Cui, Y.-L. Men, F.-F. Cao, S.-H. Yu, J. B. Goodenough, Photocatalytic CO$_2$ reduction by carbon-coated indium-oxide nanobelts, J. Am. Chem. Soc. 139 (2017) 4123–4129, https://doi.org/10.1021/jacs.8b00266.

[40] Y. Lin, L. Yang, Y. Zhang, H. Jiang, Z. Xiao, C. Wu, G. Zhang, J. Jiang, L. Song, Defective carbon-CoP nanoparticles hybrids with interfacial charges polarization for efficient bifunctional oxygen electrocatalysis, Adv. Energy Mater. 8 (2018) 1703623, https://doi.org/10.1002/aenm.201703623.

[41] C. Li, Y. Liu, Z. Zhuo, H. Ju, D. Li, Y. Guo, X. Wu, H. Li, T. Zhai, Local charge distribution engineered by schottky heterojunctions toward urea electrolysis, Adv. Energy Mater. 8 (2018) 1801775, https://doi.org/10.1002/aenm.201801775.

[42] C. Wang, H. Lu, Z. Mao, C. Yan, G. Shen, X. Wang, Bimetal schottky heterojunction boosting energy-saving hydrogen production from alkaline water via urea electrocatalysis, Adv. Funct. Mater. 30 (2020) 2000556, https://doi.org/10.1002/adfm.202000556.

[43] X. Wang, S. Li, Z. Yuan, Y. Sun, Z. Tang, X. Gao, H. Zhang, J. Li, S. Wang, D. Yang, J. Xie, Z. Yang, Y. Yan, Optimizing electrocatalytic nitrogen reduction via interfacial electric field modulation: elevating d-band center in WS$_2$-WO$_3$ for enhanced intermediate adsorption, Angew. Chem. Int. Ed. 62 (2023) e202303794, https://doi.org/10.1002/anie.202303794.

[44] Y. Guo, W. Shi, Y. Zhu, Y. Xu, F. Cui, Enhanced photoactivity and oxidizing ability simultaneously via internal electric field and valence band position by crystal structure of bismuth oxyiodide, Appl. Catal. B 262 (2020) 118262, https://doi.org/10.1016/j.apcatb.2019.118262.

[45] L. Zhai, X. She, L. Zhuang, Y. Li, R. Ding, X. Guo, Y. Zhang, Y. Zhu, K. Xu, H.J. Fan, S.P. Lau, Modulating built-in electric field via variable oxygen affinity for robust hydrogen evolution reaction in neutral media, Angew. Chem. Int. Ed. 61 (2022) e202116057, https://doi.org/10.1002/anie.202116057.

[46] S. Yao, S. Wang, J. Wang, Z. Hou, X. Gao, Y. Liu, W. Fu, K. Nie, J. Xie, Z. Yang, Y. Yan, Activation of MnO$_6$ units via an interfacial electric field: electron injection into Mn t$_{2g}$ for rapid and stable sodium ion storage in CeO$_2$/MnO$_x$, Small (2024) 2307482, https://doi.org/10.1002/smll.202307482.

[47] D. Voiry, M. Chhowalla, Y. Gogotsi, N.A. Kotov, Y. Li, R.M. Penner, R.E. Schaak, P. S. Weiss, Best practices for reporting electrocatalytic performance of nanomaterials, ACS Nano 12 (2018) 9635–9638, https://doi.org/10.1021/acsnano.8b07700.

[48] H. Zhang, T. Yang, H. Zhou, Y. Wang, X. Yang, W. Liang, D. Wu, P. Yuan, T. Yu, M. He, W. Wei, Activating Fe activity and improving Ni activity via C$_3$N$_4$ substrate in alkaline oxygen evolution catalyzed by Ni-Fe phosphide, Appl. Catal. B 342 (2024) 123391, https://doi.org/10.1016/j.apcatb.2023.123391.

[49] C. Wan, J. Jin, X. Wei, S. Chen, Y. Zhang, T. Zhu, H. Qu, Inducing the SnO$_2$-based electron transport layer into NiFe LDH/NF as efficient catalyst for OER and methanol oxidation reaction, J. Mater. Sci. Technol. 124 (2022) 102–108, https://doi.org/10.1016/j.jmst.2022.01.022.

[50] H. Liao, G. Ni, P. Tan, Y. Liu, K. Chen, G. Wang, M. Liu, J. Pan, Borate narrowed band gap of nickel-iron layer double hydroxide to mediate rapid reconstruction kinetics for water oxidation, Appl. Catal. B 317 (2022) 121713, https://doi.org/10.1016/j.apcatb.2022.121713.

[51] J. Zhang, Y. Ye, Z. Wang, Y. Xu, L. Gui, B. He, L. Zhao, Probing dynamic self-reconstruction on perovskite fluorides toward ultrafast oxygen evolution, Adv. Sci. 9 (2022) 2201916, https://doi.org/10.1002/advs.202201916.

[52] F. Froment, A. Tournié, P. Colomban, Raman identification of natural red to yellow pigments: ochre and iron-containing ores, J. Raman Spectrosc. 39 (2008) 560–568, https://doi.org/10.1002/jrs.1858.

[53] Y. Li, Y. Wu, H. Hao, M. Yuan, Z. Lv, L. Xu, B. Wei, In situ unraveling surface reconstruction of Ni$_5$P$_4$@FeP nanosheet array for superior alkaline oxygen evolution reaction, Appl. Catal. B 305 (2022) 121033, https://doi.org/10.1016/j.apcatb.2021.121033.

[54] Y. Wei, L. Yi, R. Wang, J. Li, D. Li, T. Li, W. Sun, W. Hu, A unique etching-doping route to Fe/Mo Co-doped Ni oxyhydroxide catalyst for enhanced oxygen evolution reaction, Small 19 (2023) 2301267, https://doi.org/10.1002/smll.202301267.

[55] Z. Wang, Z. Qi, X. Fan, D.Y.C. Leung, J. Long, Z. Zhang, T. Miao, S. Meng, S. Chen, X. Fu, Intimately contacted Ni$_2$P on CdS nanorods for highly efficient photocatalytic H$_2$ evolution: new phosphidation route and the interfacial separation mechanism of charge carriers, Appl. Catal. B 281 (2021) 119443, https://doi.org/10.1016/j.apcatb.2020.119443.

[56] Y. Wu, Y. Li, M. Yuan, H. Hao, X. San, Z. Lv, L. Xu, B. Wei, Operando capturing of surface self-reconstruction of Ni$_3$S$_2$/FeNi$_2$S$_4$ hybrid nanosheet array for overall water splitting, Chem. Eng. J. 427 (2022) 131944, https://doi.org/10.1016/j.cej.2021.131944.